J|A|C|S
ARTICLES
Published on Web 06/06/2006

Structures, Photoluminescence, and Reversible Vapoluminescence Properties of Neutral Platinum(II) Complexes Containing Extended π-Conjugated Cyclometalated Ligands

Steven C. F. Kui, Stephen Sin-Yin Chui, Chi-Ming Che,* and Nianyong Zhu

Contribution from the Department of Chemistry, Open Laboratory of Chemical Biology of the Institute of Molecular Technology for Drug Discovery and Synthesis, and HKU-CAS Joint Laboratory on New Materials, The University of Hong Kong, Pokfulam Road, Hong Kong SAR, China

Received March 1, 2006; E-mail: cmche@hku.hk

Abstract: Reacting K_2PtCl_4 with the tridentate R-C^N^C-H_2 ligands 2,6-di-(2′-naphthyl)-4-R-pyridine (R = H, **1a**; Ph, **1b**; 4-BrC_6H_4, **1c**; 3,5-$F_2C_6H_3$, **1d**) in glacial acetic acid, followed by heating in dimethyl sulfoxide (DMSO), gave complexes [(R-C^N^C)Pt(DMSO)] (**2a**−**d**). In the crystal structures of **2a**−**c**, the molecules are paired in a head-to-tail orientation with Pt···Pt separations >6.3 Å, and there are extensive close C−H···π (d = 2.656−2.891 Å), π···π (d = 3.322−3.399 Å), and C−H···O═S (d = 2.265−2.643 Å) contacts. [(Ph-C^N^C)Pt(PPh_3)] (**3**) was prepared by reacting **2b** with PPh_3. Reactions of **2a**−**d** with bis(diphenylphosphino)-methane (dppm) gave [(R-C^N^C)$_2$Pt$_2$(μ-dppm)] (**4a**−**d**). Both head-to-head (syn) and head-to-tail (anti) conformations were found for **4a**·6$CHCl_3$·C_5H_{12}, whereas only one conformation was observed for **4b**·2$CHCl_3$ (syn), **4c**·3CH_2Cl_2 (syn), and **4d**·2$CHCl_3$ (anti). In the crystal structures of **4a**−**d**, there are close intramolecular Pt···Pt contacts of 3.272−3.441 Å in the syn conformers, and long intramolecular Pt···Pt separations of 5.681−5.714 Å in the anti conformers. There are weak C−H···X (d = 2.497−3.134 Å) and X···X (X = Cl or Br; d = 2.973−3.655 Å) interactions between molecules **4a**−**d** and occluded $CHCl_3$/CH_2Cl_2 molecules, and their solvent channels are of varying diameters (~9−28 Å). Complexes **2a**−**d**, **3**, and **4a**−**d** are photoluminescent in the solid state, with emission maxima at 602−643 nm. Upon exposure to volatile organic compounds, **4a** shows a fast and reversible vapoluminescent response, which is most intense with volatile halogenated solvents (except CCl_4). Powder X-ray diffraction analysis of desolvated **4a** revealed a more condensed molecular packing of syn and anti complexes than crystal **4a**·6$CHCl_3$·C_5H_{12}.

Introduction

Non-covalent C−H···π and π···π interactions are weaker in energy than conventional H-bonds involving O and/or N atom donors.[1] These weak interactions are instrumental in the organization of small molecules into supermolecules[2−6] and in the self-assembly conformational dynamics of macromolecules such as nucleic acids and proteins.[7−12] In contemporary metal−organic coordination chemistry, C−H···π and π···π interactions have been exploited to create a diverse number of supramolecular architectures, such as catenanes, rotaxanes, knots, ribbons, and cages.[13] They also influence inter- and intramolecular metal−metal and ligand−ligand interactions as well as solid-state photoluminescence properties, particularly those involving square planar Pt(II) complexes containing π-conjugated N- and/or C-donor ligands.[14−23]

Vapoluminescent materials that are capable of detecting volatile organic compounds (VOCs) with fast response times have many potential practical applications. In the literature,

(1) Jorgensen, W. L.; Severance, D. L. *J. Am. Chem. Soc.* **1990**, *112*, 4768−4774.
(2) (a) Amabilino, D. B.; Stoddart, J. F. *Chem. Rev.* **1995**, *95*, 2725−2828. (b) Claessens, C. G.; Stoddart, J. F. *J. Phys. Org. Chem.* **1997**, *10*, 254−272.
(3) Hirsch, K. A.; Wilson, S. R.; Moore, J. S. *Chem. Eur. J.* **1997**, *3*, 765−771.
(4) (a) Lightfoot, M. P.; Mair, F. S.; Pritchard, R. G.; Warren, J. W. *Chem. Commum.* **1999**, 1945−1946. (b) Brown, S. P.; Schnell, I.; Brand, J. D.; Mülen, K.; Spiess, H. W. *J. Am. Chem. Soc.* **1999**, *121*, 6712−6718. (c) Lämsü, M.; Huuskonen, J.; Rissanen, K.; Pursiainen, J. *Chem. Eur. J.* **1998**, *4*, 84−92. (d) Dance, I.; Scudder, M. *Chem. Eur. J.* **1996**, *2*, 481−486.
(5) Chipot, C.; Jaffe, R.; Maigret, B.; Pearlman, D. A.; Kollman, P. A. *J. Am. Chem. Soc.* **1996**, *118*, 11217−11224.
(6) Hunter, C. A. *Chem. Soc. Rev.* **1994**, 101−109.
(7) Burley, S. K.; Petsko, G. A. *J. Am. Chem. Soc.* **1986**, *108*, 7995−8001.
(8) Hunter, C. A.; Singh, J.; Thornton, J. M. *J. Mol. Biol.* **1991**, *218*, 837−846.
(9) Serrano, L.; Bycroft, M.; Fersht, A. R. *J. Mol. Biol.* **1991**, *218*, 465−475.
(10) Burley, S. K.; Petsko, G. A. *Science* **1985**, *229*, 23−28.
(11) Guckiau, K. M.; Schweitzer, B. A.; Ren, R. X.-F.; Sheils, C. J.; Tahmassebi, D. C.; Kool, E. T. *J. Am. Chem. Soc.* **2000**, *122*, 2213−2222.
(12) Müller-Dethlefs, K.; Hobza, P. *Chem. Rev.* **2000**, *100*, 143−168.
(13) (a) Raymo, F. M.; Stoddard, J. F. *Chem. Rev.* **1999**, *99*, 1643−1663. (b) Puddephatt, R. J. *Coord. Chem. Rev.* **2001**, *216−217*, 313−332. (c) Seidal, S. R.; Stang, P. J. *Acc. Chem. Res.* **2002**, *35*, 972−983. (d) Ruben, M.; Rojo, J. Romero-Salguero, F. J.; Uppadine, L. H.; Lehn, J. M. *Angew. Chem., Int. Ed.* **2004**, *43*, 3644−3662. (e) Fujita, M.; Tominaga, M.; Hori, A.; Therrien, B. *Acc. Chem. Res.* **2005**, *38*, 371−380.
(14) Buchner, R.; Cumingham, C. T.; Field, J. S.; Haines, R. J.; McMillin, D. R.; Summerton, G. C. *J. Chem. Soc., Dalton Trans.* **1999**, 711−718.
(15) Kato, M.; Kosuge, C.; Morii, K.; Ahu, J. S.; Kitagawa, H.; Mitani, T.; Matsushita, M.; Kato, T.; Yano, S.; Kimura, M. *Inorg. Chem.* **1999**, *38*, 1638−1641.

design strategies for VOC-detecting vapoluminescent materials have been based on (i) the facile reversible change of the molecular structure of the luminophore and (ii) alterations in the molecular packing when the analyte molecule enters and exits the crystal structure of the luminescent sensory material. Using strategy (i), van Koten and co-workers have reported that a non-porous crystalline Pt(II) complex [(NCN-OH)PtCl] (NCN-OH = 4-(OH)-2,6-$(CH_2NMe_2)_2$-C_6H_2) can detect SO_2 gas through a reversible Pt−S bond formation/disruption in the solid state.[19] Using strategy (ii), Mann and co-workers reported that the Magnus salts $[Pt(CNR)_4][M(CN)_4]$ (M = Pd, Pt)[20] underwent a reversible structural change upon exposure to methanol which led to vapochromic behavior. Connick and Eisenberg recently reported that the $[Pt(Me_2bzimpy)Cl]X$ ($Me_2bzimpy$ = 2,6-bis-(*N*-methylbenzimidazol-2-yl)pyridine; X = Cl or PF_6)[21] and $[Pt(Nttpy)Cl](PF_6)_2$ crystals (Nttpy = 4′-(*p*-nicotinamide-*N*-methylphenyl-2,2′:6′2″-terpyridine)[22] produced a significant color change (e.g., orange-red ↔ yellow) upon desorption/re-absorption of solvent molecules. In addition, Kato and Che reported the reversible vapoluminescent behavior of *syn*-$[Pt_2(bpy)_2(pyt)_2](PF_6)_2$ (pyt = pyridine-2-thiolate)[23a] and [(^{t}Bu$_2$-bpy)Pt(C≡CR)$_2$] (R = C_5H_4N, C_6F_5)[23c] solids upon exposure to MeCN,[23a] EtOH,[23a] and halogenated VOCs.[23c] They attributed the reversible vapoluminescent behavior to crystal packing effects, the presence of well-defined solvent channels, and non-covalent weak interactions between the platinum complex and the VOCs.

The study of the spectroscopic and photophysical properties of cyclometalated Pt(II) complexes is an area of considerable interest.[24] Neutral Pt(II) complexes with the cyclometalated 2,6-diphenylpyridine ligand (C^N^C-H_2) (Chart 1) are known to possess rich photophysical properties.[25,26] Previously, we observed two polymorphic forms of [(C^N^C)$_2$Pt$_2$(μ-dppm)] (orange and yellow);[27a] the orange form changed reversibly to a yellow form upon exposure to VOCs (CH_2Cl_2, acetone, etc.). The accompanying change in the emission signal (lifetime, emission energy, and intensity) was small, thus limiting the potential use of [(C^N^C)$_2$Pt$_2$(μ-dppm)] as a vapoluminescent material. We envisioned that, by using an extended π-conjugated cyclometalating ligand such as 2,6-di-(2′-naphthyl)-4-R-pyridine (R-C^N^C-H_2), the non-covalent C−H···π and π···π interactions between the cyclometalated ligands and VOCs would be significantly enhanced, and hence the change in emission signal associated with the disruption of these weak interactions may be amplified. Here we describe the synthesis of the R-C^N^C-H_2 ligands **1a**−**d** and their Pt(II) complexes **2**−**4** (Chart 1). We show that the crystal structure of **4a**·6$CHCl_3$·C_5H_{12} has large accessible solvent channels (ca. 6.5 × 4.3 Å^2), and its desolvated form exhibits a facile and reversible vapoluminescent response upon exposure to VOCs. Comparative powder X-ray diffraction (PXRD) studies revealed that the desolvation of crystal **4a** led

Chart 1. Neutral Cyclometalated Pt(II) Complexes [(C^N^C)Pt(L)] (Upper Right) and Naphthyl-Substituted Analogues [(R-C^N^C)Pt(L)] (Upper Left and Bottom, Described in This Work)[a]

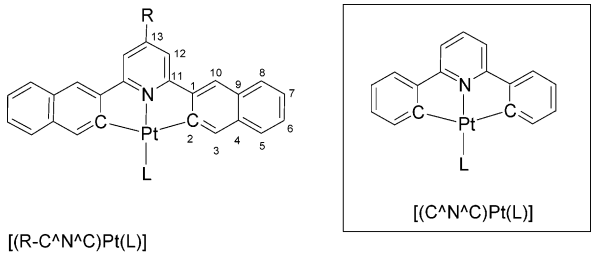

[(R-C^N^C)Pt(L)]
L = DMSO: R = H, **2a**; Ph, **2b**; 4-BrC_6H_4, **2c**; 3,5-$F_2C_6H_3$, **2d**
L = PPh_3: R = Ph, **3**

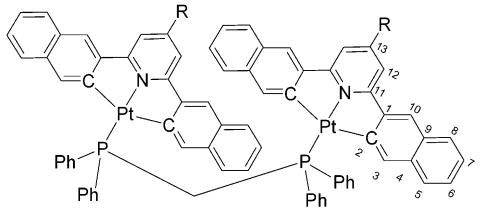

[(R-C^N^C)$_2$Pt$_2$(μ-dppm)]
R = H, **4a**; Ph, **4b**; 4-BrC_6H_4, **4c**; 3,5-$F_2C_6H_3$, **4d**

[a] Numbers 1−13 on the carbon atoms were added for ^{1}H NMR assignment.

(16) (a) Houlding, V. H.; Miskowski, V. M. *Coord. Chem. Rev.* **1991**, *111*, 145−152. (b) Chan, C. W.; Cheng, L. K.; Che, C.-M. *Coord. Chem. Rev.* **1994**, *132*, 87−97. (c) Connick, W. B.; Geiger, D.; Eisenberg, R. *Inorg. Chem.* **1999**, *38*, 3264−3265. (d) Yip, H. K.; Cheng, L. K.; Cheung, K. K.; Che, C.-M. *J. Chem. Soc., Dalton Trans.* **1993**, 2933−2938. (e) Aldridge, T. K.; Stacy, E. M.; McMillin, D. R. *Inorg. Chem.* **1994**, *33*, 722−727. (f) Arena, G.; Calogero, G.; Campagna, S.; Scolaro, L. M.; Ricevuto, V.; Romeo, R. *Inorg. Chem.* **1998**, *37*, 2763−2769. (g) Cheung, T. C.; Cheung, K. K.; Peng, S. M.; Che, C.-M. *J. Chem. Soc., Dalton Trans.* **1996**, 1645−1652. (h) Lai, S. W.; Chan, M. C. W.; Cheung, T. C.; Peng, S. M.; Che, C.-M. *Inorg. Chem.* **1999**, *38*, 4046−4055. (i) Lai, S. W.; Chan, M. C. W.; Cheung, K. K.; Che, C.-M. *Inorg. Chem.* **1999**, *38*, 4262−4267.

(17) (a) Lippard, S. J. *Acc. Chem. Res.* **1978**, *11*, 211−217. (b) Barton, J. K.; Lippard, S. J. *Biochemistry* **1979**, *18*, 2661−2668. (c) Howe-Grant, M.; Lippard, S. J. *Biochemistry* **1979**, *18*, 5762−5769. (d) Dewan, J. C.; Lippard, S. J.; Bauer, W. R. *J. Am. Chem. Soc.* **1980**, *102*, 858−860. (e) Liu, H. Q.; Cheung, T. C.; Peng, S. M.; Che, C.-M. *J. Chem. Soc., Chem. Commun.* **1995**, 1787−1788. (f) Liu, H. Q.; Cheung, T. C.; Che, C.-M. *J. Chem. Soc., Chem. Commun.* **1996**, 1039−1040. (g) Ma, D. L.; Che, C.-M. *Chem. Eur. J.* **2003**, *9*, 6133−6144.

(18) Ratilla, E. M. A.; Brothers, H. M., II; Kostic, N. M. *J. Am. Chem. Soc.* **1987**, *109*, 4592−4599.

(19) (a) Albrecht, M.; Lutz, M.; Spek, A. L.; van Koten, G. *Nature* **2000**, *406*, 970−974. (b) Albrecht, M.; Gossage, R. A.; Lutz, M.; Spek, A. L.; van Koten, G. *Chem. Eur. J.* **2000**, *6*, 1431−1445.

(20) (a) Daws, C. A.; Exstrom, C. L.; Sowa, J. R.; Mann, K. R. *Chem. Mater.* **1997**, *9*, 363−368. (b) Kunugi, Y.; Mann, K. R.; Miller, L. L.; Exstrom, C. L. *J. Am. Chem. Soc.* **1998**, *120*, 589−590. (c) Exstrom, C. L.; Pomije, M. K.; Mann, K. R. *Chem. Mater.* **1998**, *10*, 942−945. (d) Kunugi, Y.; Miller, L. L.; Mann, K. R.; Pomije, M. K. *Chem. Mater.* **1998**, *10*, 1487−1489. (e) Buss, C. E.; Anderson, C. E.; Pomije, M. K.; Lutz, C. M.; Britton, D.; Mann, K. R. *J. Am. Chem. Soc.* **1998**, *120*, 7783−7790. (f) Buss, C. E.; Mann, K. R. *J. Am. Chem. Soc.* **2002**, *124*, 1031−1039.

(21) Grove, L. J.; Rennekamp, J. M.; Jude, H.; Connick, W. B. *J. Am. Chem. Soc.* **2004**, *126*, 1594−1595.

(22) Wadas, T. J.; Wang, Q. M.; Kim, Y. J.; Flaschenreim, C.; Blanton, T. N.; Eisenberg, R. *J. Am. Chem. Soc.* **2004**, *126*, 16841−16849.

(23) (a) Kato, M.; Omura, A.; Toshikawa, A.; Kishi, S.; Sugimoto, Y. *Angew. Chem., Int. Ed.* **2002**, *41*, 3183−3185. (b) Che, C.-M.; Fu, W. F.; Lai, S. W.; Hou, Y. J.; Liu, Y. L. *Chem. Commun.* **2003**, 118−119. (c) Lu, W.; Chan, M. C. W.; Zhu, N.; Che, C.-M.; He, Z.; Wong, K. Y. *Chem. Eur. J.* **2003**, *9*, 6155−6166.

(24) (a) Chassot, L.; von Zelewsky, A.; Sandrini, D.; Maestri, M.; Balzani, V. *J. Am. Chem. Soc.* **1986**, *108*, 6084−6085. (b) Yersin, H.; Humbs, W.; Strasser, J. *Coord. Chem. Rev.* **1997**, *159*, 3325−358. (c) Crites Tears, D. K.; McMillin, D. R. *Coord. Chem. Rev.* **2001**, *211*, 195−205. (d) Hissler, M.; Harriman, A.; Khatyr, A.; Ziessel, R. *Chem. Eur. J.* **1999**, *5*, 3366−3381. (e) Bailey, J. A.; Hill, M. G.; Marsh, R. E.; Miskowski, V. M.; Schaefer, W. P.; Gray, H. B. *Inorg. Chem.* **1995**, *34*, 4591−4599. (f) Constable, E. C.; Henney, R. P. G.; Leese, T. A. *J. Chem. Soc., Dalton Trans.* **1990**, 443−450.

(25) (a) Deuschel-Cornioley, C.; Ward, T.; von Zelewsky, A. *Helv. Chim. Acta* **1988**, *71*, 130−133. (b) Maestri, M.; Deuschel-Cornioley, C.; von Zelewsky, A. *Coord. Chem. Rev.* **1991**, *111*, 117−123. (c) Yam, V. W. W.; Tang, R. P. L.; Wong, K. M. C.; Lu, X. X.; Cheung, K. K.; Zhu, N. *Chem. Eur. J.* **2002**, *8*, 4066−4076.

(26) Wong, K. H.; Cheung, K. K.; Chan, M. C. W.; Che, C.-M. *Organometallics* **1998**, *17*, 3505−3511.

(27) (a) Lu, W.; Chan, M. C. W.; Cheung, K. K.; Che, C.-M. *Organometallics* **2001**, *20*, 2477−2486. (b) Lu, W.; Zhu, N.; Che, C.-M. *Chem. Commum.* **2002**, 900−901.

to a more condensed packing of the molecules, which was stabilized by extensive intra-/intermolecular C−H···π and π···π interactions.

Experimental Section

General. Instrumentation methods used for characterization of the newly prepared platinum(II) complexes, photophysical and spectroscopic studies, and structure determination by X-ray single-crystal analysis are described in the Supporting Information.[28−31]

[(R-C^N^C)Pt(DMSO)] (2a−d). A modification of Rourke's method was employed.[30] A mixture of K_2PtCl_4 and the R-C^N^C-H_2 ligand in glacial acetic acid (100 mL) was refluxed for 48 h to afford a yellow suspension. The yellow precipitate was collected by filtration and washed with water and acetone. The solid was redissolved in boiling dimethyl sulfoxide (DMSO) to give a clear solution. Water (10 mL) was added to precipitate the complex as a yellow solid. The solid was purified by column chromatography (neutral alumina, CH_2Cl_2 as eluent). Yellow crystals of **2a**, **2b**·$CHCl_3$, and **2c**·$2CH_2Cl_2$ were obtained by slow evaporation of chloroform solutions.

[(Ph-C^N^C)Pt(PPh$_3$)] (3). A mixture of **2b** (0.064 g, 0.09 mmol) and PPh_3 (0.025 g, 0.09 mmol) in dry dichloromethane (20 mL) was stirred under a N_2 atmosphere at room temperature for 12 h. The resultant mixture was evaporated to dryness and purified by column chromatography (neutral alumina, CH_2Cl_2/*n*-hexane (1:1) as eluent) to give **3** as a golden yellow crystalline solid.

[(R-C^N^C)$_2$Pt$_2$(μ-dppm)] (4a−d). A mixture of **2a** and dppm (0.5 equiv) in dry dichloromethane (20 mL) was stirred under N_2 at room temperature for 12 h. The reaction mixture was evaporated to dryness to afford **4a**, which was purified by column chromatography (neutral alumina, CH_2Cl_2/*n*-hexane (1:1) as eluent). Complexes **4b**−**d** were similarly prepared from **2b**−**d** using the same procedure.

Structure Determination by Powder X-ray Diffraction. A ground fine powder sample of **4a** was predried under vacuum overnight. The sample was side-loaded onto a flat glass holder. PXRD data were collected on a Philips PW3710 diffractometer ($\theta/2\theta$) with X-ray radiation (CuK$\alpha_{1,2}$, $\lambda = 1.5406$ Å, 40 kV and 40 mA, Ni foil filtered, graphite crystal as a diffracted beam monochromator). Fixed divergence ($^1/_4°$), anti-scatter ($^1/_4°$), and receiving (0.1 mm) slits were used. Step-scanned data collection was performed in the 2θ range of 3−50° with a step size of 0.02° and a scan speed of 0.004° s^{-1}. A simulated PXRD pattern was calculated using the PowderCell[32] program based on the atomic coordinates and unit cell parameters derived from single-crystal X-ray data. Initial unit cell parameters of **4a** were obtained by indexing the first 20 peak positions of its PXRD pattern via the DICVOL91[33a] program ($a = 15.0625$ Å, $b = 20.8286$ Å, $c = 22.2975$ Å; $\alpha = 64.237°$, $\beta = 71.595°$, $\gamma = 75.051°$; $V = 5917.9$ Å^3), with figures of merit[33b] $M(20)$ and $F(20)$ of 10.1 and 35.8, respectively. Subsequent Rietveld analysis gave the final unit cell parameters listed in Table 4. Based on the results of elemental analyses and ^{1}H, ^{31}P{^{1}H}, and ^{195}Pt NMR spectra, the chemical connectivities of [(R-C^N^C)$_2$Pt$_2$(μ-dppm)] complexes in the desolvated and solvated forms of **4a** were shown to be the same. Based on the unit cell volume, there are two molecules per asymmetric unit ($Z = 2$) for a triclinic space group $P\bar{1}$. The refined unit cell volume (6188 Å^3) is comparable to the expected value of 6046 Å^3, where all solvent molecules were removed from the crystal lattice of solvated **4a**·$6CHCl_3$·C_5H_{12}. The desolvated structural model for desolvated **4a** was constructed on the basis of the bond distances and angles derived from single-crystal data of **4a**·$6CHCl_3$·C_5H_{12}. A total of 300 bond distance restraints and 720 bond angle restraints of weighing factors of 1000 were used to initiate the Rietveld restrained refinement using the GSAS/EXPGUI programs.[34] Twenty-eight planar restraints for the eight phenyl rings of the two dppm ligands and the four [(R-C^N^C)Pt] entities were used to constrain the planarity of these groups. The molecular orientations of the *syn*- and *anti*-[(R-C^N^C)$_2$Pt$_2$(μ-dppm)] complexes were refined so as to optimize the packing efficiency. Any unrealistic intermolecular contacts were avoided and sequentially removed by applying appropriate atom−atom distance restraints (typically, the minimum non-bonded distances for H···H and C···H are ca. 2.00 and 2.60 Å, respectively). Structure refinement was performed by Rietveld profile fitting of background, scale factor, polarization, and sample displacement/transparency effects. Peak shape and asymmetry were described by pseudo-Voigt coefficients.[35a,b] The systematic errors in diffraction intensity due to a preferred orientation effect of sample were corrected on the crystallographic face {111} using the March−Dollase equation[35c,d] (aspect ratio = 2.05(1) indicates a plate-like crystal habit). Unit cell parameters and all atomic coordinates were refined to give final R_p values of 7.97%, wR_p values of 11.2%, goodness-of-fit of 2.13, and a final (shift/esd)^2 of 0.04.

Solid-State Emission Quantum Yield (Φ_{ss}). Emission quantum yields (Φ_{ss}) of solid samples upon exposure to VOCs under saturation conditions were determined by the method of Wrighton[36] [$\Phi_{ss} = E/(R_{std} - R_{smpl})$] using KBr as a reference. At a given excitation wavelength, E refers to the area of the corrected emission spectrum, and R_{std} and R_{smpl} refer to the area of the diffuse reflectance curve of the non-absorbing standard (KBr) and sample, respectively. The desolvated solid (**4**) was packed in a sample holder ($0.5 \times 1.0 \times 0.2$ cm^3) and exposed to VOCs for 10 min to allow equilibration. The whole setup was covered by a quartz slide, and the emission intensity was recorded and calibrated with the diffuse reflectance curves of the non-absorbing standard (KBr) at $\lambda_{ex} = 700$ nm.

Results and Discussion

In previous work, the crystal structure of the orange crystalline form of [(C^N^C)$_2$Pt$_2$(μ-dppm)]·$CHCl_3$[27a] (C^N^C-H_2 = 2,6-diphenylpyridine) containing the [(C^N^C)$_2$Pt$_2$(μ-dppm)] molecules was shown to adopt an anti conformation with two intramolecular π···π contacts (between the [(C^N^C)Pt] units and phenyl rings of the dppm ligand; 3.12−3.29 Å). This crystal changed to a bright yellow color upon exposure to dichloromethane, acetone, pentane, benzene, or methanol vapor. The changes in both emission maximum and lifetime between the orange and yellow forms were small. In this work, we replaced the phenyl group of C^N^C-H_2 with a naphthyl group to give a new class of π-conjugated cyclometalated ligands (R-C^N^C-H_2).

(28) (a) Kendurkar, P. S.; Tewari, R. S. *J. Chem. Eng. Data* **1974**, *19*, 184−188. (b) Silva, A. M. S.; Almeida, L. M. P. M.; Cavaleiro, J. A. S.; Foces-Foces, C.; Llamas-Saiz, A. L.; Fontenas, C.; Jagerovic, N.; Elguero, J. *Tetrahedron* **1997**, *53*, 11645−11658.
(29) Perrin, D. D.; Armarego, W. L. F.; Perrin, D. R. *Purification of Laboratory Chemicals*, 2nd ed.; Pergamon: Oxford, 1980.
(30) (a) Cave, G. W. V.; Alcock, N. W.; Rourke, J. P. *Organometallics* **1999**, *18*, 1801−1803. (b) Cave, G. W. V.; Fanizzi, F. P.; Deeth, R. J.; Errington, W.; Rourke, J. P. *Organometallics* **2000**, *19*, 1355−1364.
(31) (a) DENZO: In the HKL Manual—A description of programs DENZO, XDISPLAYF and SCALEPACK, written by D. Gewirth, with the cooperation of the program authors Z. Otwinowski and W. Minor, Yale University, New Haven, CT, 1995. (b) Altomare, A.; Burla, M. C.; Camalli, M.; Cascarano, G.; Giacovazzo, C.; Guagliardi, A.; Moliterni, A. G. G.; Polidori, G.; Spagna, R. Sir97: a new tool for crystal structure determination and refinement. *J. Appl. Crystallogr.* **1999**, *32*, 115−119. (c) Sheldrick, G. M. SHELXL97, A program for Crystal Structure Analysis (Release 97-2); University of Goetingen, Germany, 1997.
(32) Kraus, W.; Nolze, G. PowderCell for Windows, version 2.4; Federal Institute for Materials Research and Testing, Rudower Chaussee 5, 12489, Berlin, Germany.
(33) (a) Boultif, A.; Louer, D. *J. Appl. Crystallogr.* **1991**, *24*, 987−993. (b) De Wolff, P. M. *J. Appl. Crystallogr.* **1968**, *1*, 108−113.
(34) Larson, C.; von Dreele, R. B. GSAS−General Structure Analysis System; Report LAUR 86-748; Los Alamos National Laboratory: Los Alamos, NM, 1994. Toby, B. H. EXPGUI, graphical user interface for GSAS. *J. Appl. Crystallogr.* **2001**, *34*, 210−213.
(35) (a) Thompson, P.; Cox, D. E.; Hastings, J. B. *J. Appl. Crystallogr.* **1987**, *20*, 79−83. (b) Finger, L. W.; Cox, D. E.; Jephcoat, A. P. *J. Appl. Crystallogr.* **1994**, *27*, 892−900. (c) March, A. *Z. Kristallogr.* **1932**, *81*, 285−297. (d) Dollase, W. A. *J. Appl. Crystallogr.* **1986**, *19*, 267−272.
(36) Wrighton, M. S.; Ginley, D. S.; Morse, D. L. *J. Phys. Chem.* **1974**, *78*, 2229−2233.

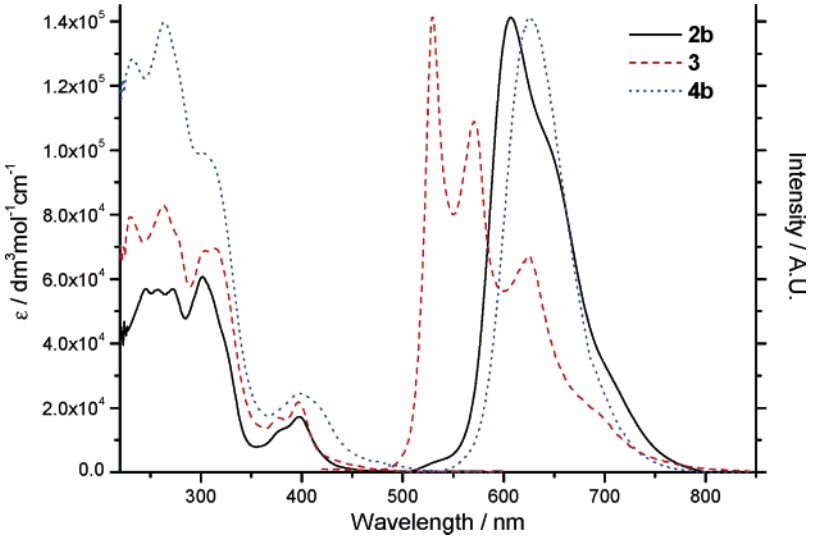

Figure 1. UV−vis absorption (in CH_2Cl_2) and solid-state emission spectra of **2b**, **3**, and **4b** at room temperature.

Table 1. UV−Vis Absorption (in CH_2Cl_2; 4×10^{-5} mol dm^{-3}) and Emission Data for **2a**−**d** and **3** (λ_{ex} = 350 nm)

		λ_{max}/nm (τ/μs)		
complex	λ_{max}/nm (ϵ/dm^3 mol^{-1} cm^{-1})[a]	solid,[b] 298 K	solid,[b] 77 K	2-MeTHF glassy solution (4×10^{-5} mol dm^{-3}), 77 K
[(C^N^C)Pt-(DMSO)][27a,30]	247 (40340), 275 (37820), 334 (14420), 346 (16660), 420 (sh, 490)	556 (0.6)	635 (1.7)	508 (21), 545, 584
2a	246 (58600), 309 (50510), 375 (11900), 392 (17160), 425 (sh, 1000)	627 (2.0)	556 (sh, 60), 592, 627	521 (1440), 565, 613
2b	246 (56980), 257 (56770), 272 (56920), 302 (60810), 398 (17280), 450 (sh, 990)	602 (8.6)	550 (70), 595, 644 (sh, 70)	521 (1670), 565, 612
2c	245 (56440), 262 (54790), 275 (59780), 302 (67380), 400 (16320), 440 (sh, 1140)	609 (8.5)	604 (31), 655	522 (720), 567, 613
2d	246 (45390), 272 (53170), 305 (47270), 404 (13640), 440 (sh, 700)	609 (3.1)	584 (sh, 70), 616	525 (610), 569, 616
3	231 (79320), 263 (82940), 303 (68760), 314 (69530), 376 (16910), 396 (21780), 450 (2270)	530 (0.5), 571 (0.5), 625 (0.5)	564 (0.7), 610 (0.7)	522 (390), 564, 615

[a] In CH_2Cl_2. [b] Desolvated form, $\Phi_{ss} < 0.01$.

Reacting K_2PtCl_4 with R-C^N^C-H_2 gave [(R-C^N^C)Pt-(DMSO)] (**2a**−**d**), which were then reacted with dppm to give [(R-C^N^C)$_2$Pt$_2$(μ-dppm)] (**4a**−**d**) in >88% yields. Similar reaction of **2b** with PPh_3 gave [(Ph-C^N^C)Pt(PPh_3)] (**3**). Complexes **2a**−**d**, **3**, and **4a**−**d** are stable in air and were purified by column chromatography. Thermogravimetric analysis revealed that **2a**−**d** decomposed at 150 °C through the loss of DMSO and were subsequently converted to metallic platinum at temperatures above 300 °C. Complexes **4a**,**c** have a decomposition temperature at ∼400 °C, whereas **4b**,**d** have a lower decomposition temperature of ∼200 °C. UV−vis absorption and solid-state emission spectra of **2b**, **3**, and **4b** at room temperature are depicted in Figure 1.

Well-resolved NMR spectra were observed for **2a**−**d**, **3**, and **4a**−**d**; assignments of the signals were based on ^{1}H−^{1}H correlation and NOESY 2-D NMR experiments. For **4a**−**d**, the methylene signals of the dppm ligand appear as a triplet of triplets with $^2J_{H-P} \approx 12$ Hz and $^3J_{H-Pt} \approx 17$ Hz. The ^{31}P{^{1}H} NMR spectra of **4a**−**d** (the spectrum of **4b** in CD_2Cl_2 is given in Figure S1a in the Supporting Information as an example) feature one intense peak with ^{195}Pt satellites ($^1J_{P-Pt} \approx 4250$ Hz) similar to those found for [(C^N^N)$_2$Pt$_2$(μ-dppm)](ClO$_4$)$_2$ (C^N^N-H = 6-phenyl-2,2′-bipyridine) (ca. 4110 Hz)[16h] and [(C^N^C)$_2$Pt$_2$(μ-dppm)] (ca. 4150 Hz).[27a] Simulation of the spectra based on an AA′XX′ system using the gNMR 4.1 program[39] (Figures S1b,c in the Supporting Information) indicates that **4a**−**d** adopt a syn conformation (with intramolecular Pt···Pt interactions) in solution at room temperature. When the temperature was decreased from 0 to −80 °C, the signals (in CD_2Cl_2 and deuterated 2-MeTHF solutions) were broadened and could not be resolved.

Absorption and Emission Spectroscopy. UV−vis spectral data of **2a**−**d** and **3** are listed in Table 1. Their absorption spectra show peak maxima at ∼246, ∼302, and ∼400 nm, with $\epsilon > 10^4$ dm^3 mol^{-1} cm^{-1}, with a broad absorption appearing at 420−460 nm ($\epsilon < 3000$ dm^3 mol^{-1} cm^{-1}). There is a small solvatochromic shift (±5 nm) in the absorption spectra of **2a**−**d** and **3** upon changing the solvent from CH_2Cl_2 to 2-MeTHF or

(37) (a) Desiraju, G. R. *Acc. Chem. Res.* **2002**, *35*, 565−573. (b) Parsch, J.; Engels, J. W. *J. Am. Chem. Soc.* **2002**, *124*, 5664−5672. (c) Caminati, W.; Melandri, S.; Moreachini, P.; Favero, P. G. *Angew. Chem., Int. Ed.* **1999**, *38*, 2924−2925. (d) Kui, S. C. F.; Zhu, N.; Chan, M. C. W. *Angew. Chem., Int. Ed.* **2003**, *42*, 1628−1632. (e) Chan, M. C. W.; Kui, S. C. F.; Cole, J. M.; McIntyre, G. J.; Matsui, S.; Zhu, N.; Tam, K. H. *Chem. Eur. J.* **2006**, *12*, 2607−2619.
(38) Spek, A. L. PLATON, A Multipurpose Crystallographic Tool. *J. Appl. Crystallogr.* **2003**, *36*, 7−13.
(39) Budzelaar, P. H. M. *gNMR version 4.1.0.*; Cherwell Scientific Publishing: California, 1999.

Table 2. UV−Vis Absorption (in CH_2Cl_2; 4×10^{-6} mol dm^{-3}) and Emission Data for **4a**−**d** ($\lambda_{ex} = 350$ nm)

		λ_{max}/nm (τ/μs)			
complex	λ_{max}/nm (ϵ/dm^3 mol^{-1} cm^{-1})[a]	solid,[b] 298 K	solid,[b] 77 K	2-MeTHF glassy solution (4×10^{-5} mol dm^{-3}),77 K	Φ_{ss}
[(C∧N∧C)$_2$Pt$_2$-(μ-dppm)][27a]	250 (58900), 280 (45620), 350 (18920), 430 (sh, 1520), 490 (sh, 320)	624 (0.25)	633 (4.4)	525 (13), 604 (9.1)	<0.01
4a	249 (117050), 309 (85790), 388 (23360), 450 (sh, 3130)	602 (1.0)	614 (3.7)	521 (990), 566, 614 (740)	<0.01
4b	232 (129710), 264 (141240), 301 (sh, 100490), 398 (25840), 476 (sh, 3770)	627 (1.3)	636 (2.5)	522 (490), 536, 568, 616 (470)	0.15
4c	232 (111410), 271 (118250), 304 (sh, 94510), 401 (20160), 490 (sh, 3730)	643 (0.9)	692 (1.3)	538 (400), 570, 581 (400), 629	0.13
4d	234 (119390), 266 (129110), 310 (sh, 80600), 407 (21510), 492 (sh, 3970)	640 (0.6)	656 (0.9)	540 (340), 584 (340), 634	<0.01

[a] In CH_2Cl_2. [b] Desolvated form.

MeCN. UV−vis absorption (in CH_2Cl_2) and solid-state emission spectra of **2b**, **3**, and **4b** at room temperature are depicted in Figure 1.

Emission data are given in Table 1. Complexes **2a**−**d** and **3** are emissive in the solid state at 298 K and as a glassy solution in 2-MeTHF at 77 K, but they are non-emissive in fluid solutions at 298 K. The solid-state emissions of **2a**−**d** are broad, with $\lambda_{max} = 602-627$ nm, and the emissions become vibronically resolved at similar wavelengths upon cooling to 77 K. These solid-state emissions are attributed to excimeric $^3\pi\pi^*$ excited states, the energies of which are affected by intermolecular Pt···Pt and ligand−ligand interactions. Similar excimeric emissions at ~600 nm have previously been reported for [(N^N^N)-PtCl]ClO_4[24e] (N^N^N = 2,2′:6′,2"-terpyridine) and [(C^N^N)-Pt(PPh$_3$)]ClO_4[16g] crystals, both of which have intermolecular $\pi-\pi$ stacking distances of 3.33−3.39 Å. Complex **3** exhibits a vibronically structured solid-state emission with peak maxima at 530, 571, and 625 nm at room temperature. This emission band is attributed to the intraligand $^3\pi\pi^*$ excited state. At 77 K, glassy solutions of **2a**−**d** and **3** in 2-MeTHF (at concentrations ranging from 4×10^{-3} to 4×10^{-6} mol dm^{-3}) display a vibronically structured emission with peak maxima at ca. 523 and 567 nm. The vibrational spacings are ca. 1400−1500 cm^{-1}, corresponding to C═C/C═N stretchings of the (R-C^N^C) ligands. The emission is not excimeric in nature, as there is no dependence of the emission energy on the Pt(II) complex concentration from 4×10^{-3} to 4×10^{-6} mol dm^{-3}. Consequently, an intraligand $^3\pi\pi^*$ excited state is assigned.

The UV−vis spectral data for **4a**−**d** are listed in Table 2. The absorption spectra for **4a**−**d** show vibronically structured bands with peak maxima in the range of 305−420 nm ($\epsilon > 2 \times 10^4$ dm^3 mol^{-1} cm^{-1}) and spacings ca. 1300 cm^{-1}. These absorption bands were assigned to spin-allowed intraligand ($\pi \rightarrow \pi^*$) transitions. The difference spectrum obtained by subtracting the spectrum of **4b** from that of **2b** (enlarged by a factor of 2) revealed an absorption shoulder at 425 nm with a tailing from 450 to 492 nm ($\epsilon = 3000-4000$ dm^3 mol^{-1} cm^{-1}). As this absorption was red-shifted from the absorption spectrum of monomeric [(Ph-C^N^C)Pt(PPh$_3$)] (**3**), we assigned it to the excimeric $^3\pi\pi^*$ excited state as a result of intramolecular interaction between the [(R-C^N^C)Pt] moieties in [(R-C^N^C)$_2$Pt$_2$(μ-dppm)]. The UV absorption bands at ~400 nm for **4a**−**d** underwent a very small solvatochromic shift upon changing the solvent from CH_2Cl_2 to 2-MeTHF or MeCN.

The solid-state emission data for **4a**−**d** are also depicted in Table 2. At 298 K, the complexes show an intense emission, with $\lambda_{max} = 602-643$ nm. Upon cooling to 77 K, their emissions remained broad, with λ_{max} values red-shifted to 614−692 nm. We attributed the emissions to excimeric $^3\pi\pi^*$ excited states, due to the close intramolecular contacts between the [(R-C^N^C)Pt] moieties. In the crystal structure of **4d**, there are no close Pt···Pt contacts and the interplanar separation between two [(3,5-F$_2$C$_6$H$_3$-C^N^C)] planes of the two different molecules is ~3.6 Å; therefore, we attribute the emissions to an intermolecular excimeric $^3\pi\pi^*$ excited state. Diluted (~6×10^{-5} mol dm^{-3}) glassy solutions (in 2-MeTHF) of **4a**−**d** exhibited a vibronically structured emission, with $\lambda_{max} = 530-570$ nm, similar to the intraligand $^3\pi\pi^*$ emission of **2a**−**d** and **3**. There was no change in the emission energy when the concentration was increased to 6×10^{-3} mol dm^{-3}.

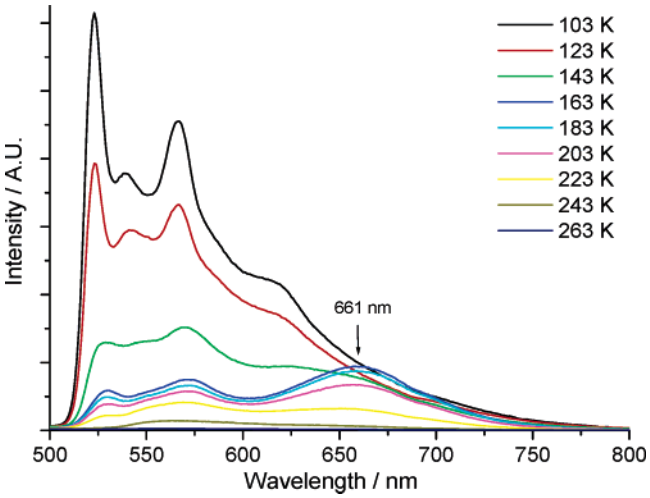

Figure 2. Emission spectra (excited at $\lambda_{ex} = 350$ nm) of **4b** in 2-MeTHF solution (4×10^{-5} mol dm^{-3}) at 103−263 K.

The emission maxima of glassy solutions of **4a**−**d** in 2-MeTHF (even at a concentration of 4×10^{-6} mol dm^{-3}) are temperature-dependent. As the temperature increases from 103 to 263 K, there is a gradual emission color change (bright green → orange → red → non-emissive). This emission spectral change can be reversed by cooling the solution from room temperature to 103 K (i.e., non-emissive → red → orange → bright green). The emission spectra of a diluted 2-MeTHF solution of **4b** (4×10^{-5} mol dm^{-3}) at various temperatures are plotted in Figure 2. At 103 K, the green emission is vibronically structured, with peak maxima at 523, 566, and 615 nm, and there is a weak and broad emission at ~660 nm. Upon raising the temperature from 103 to 163 K, the green emission

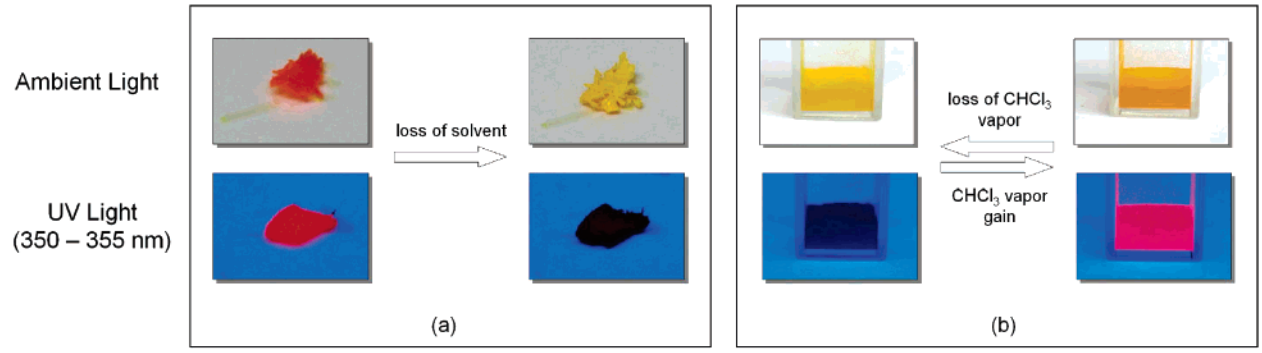

Figure 3. Solid **4a** under ambient light and under UV light irradiation (350 nm). (a) Orange crystals of **4a** upon exposure to air. (b) A reversible vapoluminescence for the desolvated form of **4a** within 1 min of being exposed to $CHCl_3$ vapor.

diminishes and a red emission (λ_{max} = 661 nm) becomes apparent: both emissions subsequently vanish as the temperature increases to 263 K. At temperatures from 103 to 163 K, the variation of the emission intensity at 661 nm is small compared with those at 523 and 566 nm (Figure S2 in the Supporting Information). The other dinuclear complexes, **4a**,**c**,**d**, exhibit similar temperature-dependent emission spectra. In contrast, 2-MeTHF glassy solutions of the monomeric congeners (i.e., **2a**−**d** and **3**) show only a green emission at 163−103 K. We found that the emission spectral changes were not sensitive to the concentrations of **4a**−**d**, suggesting that intermolecular phenomena via metal−metal and/or ligand−ligand interactions were unlikely to play significant roles.

The green emission displayed in Figure 2 is reminiscent of the emission of monomeric [(R-C^N^C)Pt(DMSO)] (**2a**−**d**) and [(Ph-C^N^C)Pt(PPh_3)] (**3**) and most reasonably comes from the $^3\pi\pi^*$ excited state of the cyclometalated R-C^N^C ligand. The red emission occurs at an energy similar to that of the solid-state emission of **4a**−**c** and can be assigned to originate from the excimeric $^3\pi\pi^*$ excited state. At temperatures above 223 K, **4a**−**d** are non-emissive in fluid solution, presumably due to efficient non-radiative decay arising from (i) the molecular motion of the flexible Pt−P−CH_2−P−Pt unit and (ii) the presence of a low-lying non-emissive d−d excited state. The non-radiative decay decreases as the temperature decreases, and at temperature ≤163 K, both the red and green emissions start to develop. We suggest that the non-radiative decay of the $^3\pi\pi^*$ excited state, being at a much higher energy (green emission), has a stronger temperature dependence than that of the excimeric $^3\pi\pi^*$ excited state (red emission). Indeed, the $^3\pi\pi^*$ emission lifetime of **3** in the solid state is 0.5 μs at 298 K, which changes to 390 μs in 2-MeTHF glassy solution at 77 K. Thus, as the temperature decreases further below 163 K, the intensity of the green emission outweighs that of the red emission and becomes dominant in the emission spectrum. At this juncture, we cannot exclude the possibility that complexes **4a**−**d** adopt more than one conformation at 103−263 K, and the green emission comes from the conformation having no intramolecular interactions. We noted that, for a 2-MeTHF solution of **4b** at 163 K, the excitation spectrum of the green emission is different from that of the red emission (the most intense peak in the former is blue-shifted by ~1020 cm^{-1} from that in the latter).

Vapoluminescent Behavior of 4a. Complex **4a** displays vapoluminescent behavior, whereas the other Pt(II) complexes do not. When a crystal of solvated **4a**·6$CHCl_3$·C_5H_{12} was removed from the mother liquor, it pulverized to a yellow translucent solid (Figure 3a). When the desolvated yellow solid (weakly emissive) was re-exposed to $CHCl_3$/CH_2Cl_2 vapor, the original bright-orange coloration was restored within several seconds (λ_{max} = 602 nm), together with an intense orange-red emission under UV irradiation (Figure 3b).

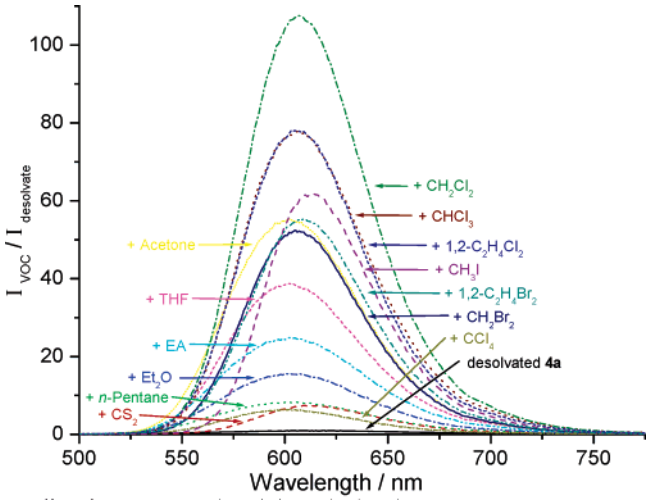

Figure 4. Effect of VOC vapors on the emission of desolvated **4a**.

Other VOCs also gave reversible vapoluminescent responses. The relative emission intensities $I_{voc}/I_{desolvate}$, where I_{voc} is the emission intensity of desolvated **4a** upon exposure to VOC under saturation conditions and $I_{desolvate}$ is the emission intensity of desolvated **4a**, are plotted in Figure 4. There is a linear correlation between the relative emission intensity and the solid-state quantum yield of desolvated **4a** upon exposure to VOCs under saturating conditions (data shown in the Supporting Information, Figure S3). The emission intensity of desolvated **4a** is dramatically enhanced in the presence of the vapor of halogenated solvents (except CCl_4), with large $I_{voc}/I_{desolvate}$ values of 107 (dichloromethane), 78 (chloroform), 78 (1,2-dichloroethane), 55 (1,2-dibromoethane), 52 (dibromomethane), and 62 (methyl iodide). The emission signals of desolvated **4a** are also enhanced by the absorption of small polar VOCs such as acetone, THF, ethyl acetate, and Et_2O ($I_{voc}/I_{desolvate}$ = 55, 39, 25, and 16, respectively); however, the $I_{voc}/I_{desolvate}$ for Et_2O is 7 times smaller than that for CH_2Cl_2. No detectable change of the emission intensity was found in the presence of benzene, toluene, *n*-hexane, acetonitrile, methanol, or ethanol vapors.

Crystal Structures of [(R-C^N^C)Pt(DMSO)] (2a−c) and [(R-C^N^C)$_2$Pt$_2$(μ-dppm)] (4a−d). Crystallographic data for **2a**−**c** and **4a**−**d** are given in Table S1 in the Supporting

Table 3. Crystallographic Data for **4a**−**d**

	complex				
	4a·6$CHCl_3$·C_5H_{12}	**4a**·6.5C_4H_8O	**4b**·2$CHCl_3$	**4c**·3CH_2Cl_2	**4d**·2$CHCl_3$
formula	$C_{150}H_{104}N_4P_4Pt_4$·6$CHCl_3$·C_5H_{12}	$C_{150}H_{104}N_4P_4Pt_4$·6.5C_4H_8O	$C_{87}H_{60}N_2P_2Pt_2$·2$CHCl_3$	$C_{87}H_{58}Br_2N_2P_2Pt_2$·3$CH_2Cl_2$	$C_{87}H_{55}F_4N_2P_2Pt_2$·2$CHCl_3$
formula weight	3654.97	3334.28	1824.23	1998.07	1896.19
color	orange	orange	red	red	yellow
crystal size, mm^3	0.4 × 0.3 × 0.25	0.4 × 0.25 × 0.2	0.4 × 0.2 × 0.15	0.3 × 0.3 × 0.25	0.4 × 0.3 × 0.2
crystal system	triclinic	triclinic	orthorhombic	monoclinic	monoclinic
space group	$P\bar{1}$	$P\bar{1}$	*Pbca*	$P2_1/n$	$P2_1/c$
a, Å	19.297(4)	19.150(4)	17.300(4)	13.915(3)	23.752(5)
b, Å	20.031(4)	19.959(4)	18.041(4)	31.731(6)	14.840(3)
c, Å	22.204(4)	22.204(4)	46.692(9)	18.321(4)	22.983(5)
α, deg	84.07(3)	84.84(3)	90	90	90
β, deg	64.23(3)	64.75(3)	90	107.87(3)	104.71(3)
γ, deg	72.66(3)	74.04(3)	90	90	90
V, $Å^3$	7374(3)	7376(3)	14573(5)	7699(3)	7836(3)
Z	2	2	8	4	4
D_{calcd}, g cm^{-3}	1.646	1.501	1.663	1.724	1.607
μ, mm^{-1}	4.205	3.884	4.150	4.967	3.869
F(000)	3588	3326	7184	3904	3720
$2\theta_{max}$, deg	50.92	50.62	51.22	51.10	51.16
no. unique data	23188	17609	12530	13339	11235
no. obsd data for $I > 2\sigma(I)$	13102	9501	8003	9774	5871
no. variables	1610	1503	910	951	944
R^a	0.059	0.051	0.046	0.037	0.041
$R_w{}^b$	0.171	0.110	0.174	0.057	0.095
goodness-of-fit *S*	0.908	0.890	1.114	0.966	0.873
residual *ρ*, e $Å^{-3}$	+2.145, −2.834	+1.161, −2.070	+2.427, −4.720	+1.449, −1.617	+1.374, −0.787

[a] $R = \sum||F_o| - |F_c||/\sum|F_o|$ based on the number of observed data $I > 2\sigma(I)$. [b] $R_w = [\sum w(|F_o^2| - |F_c^2|)^2/\sum w|F_o^2|^2]^{1/2}$ based on the number of observed unique data.

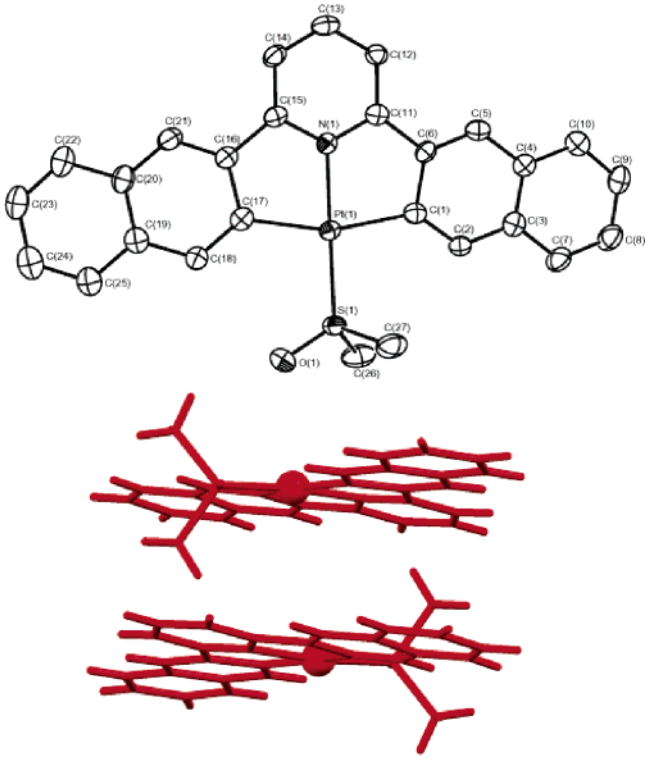

Figure 5. Perspective view of **2a** with omission of hydrogen atoms (top) and the head-to-tail pairs molecular orientation (bottom).

Information and in Table 3, respectively. The perspective view and crystal packing diagrams for **2a** are shown in Figure 5, and those of **2b** and **2c** are depicted in the Supporting Information (Figures S4 and S5). The Pt−N (2.008−2.016 Å), Pt−S (2.192−2.196 Å), and Pt−C (2.058−2.101 Å) distances are all similar to those reported for [(C^N^C)Pt(DMSO)][27a,30] and [(C^N^C)-Pt(CO)].[30] In the crystal structures of **2a**−**c**, the molecules are oriented in head-to-tail pairs with Pt···Pt separations >6.3 Å, and there are extensive intermolecular C−H···π ($d_{C-H\cdots C}$ = 2.656−2.891 Å) and $\pi\cdots\pi$ contacts ($d_{C\cdots C}$ = 3.322−3.399 Å). Other intra- and intermolecular non-covalent contact distances for **2a**−**c** and **4a**−**d** are listed in the Supporting Information (Table S2). The oxygen atom O1 of the coordinated DMSO molecule forms an intramolecular hydrogen bond with the adjacent naphthyl proton H18 and one or two intermolecular hydrogen bond(s) with neighboring molecules, such as the C−H of naphthyl group, $CHCl_3$ in **2b**, and CH_2Cl_2 in **2c**. In addition, there are weak intermolecular C−H···X and X···X interactions between the occluded solvent molecules and the Pt complexes, but no well-defined solvent channel is observed.

Complex **4a** co-crystallizes with six chloroform molecules and one *n*-pentane molecule, and both the syn and anti conformations of **4a** are present in the crystal structure of **4a**·6$CHCl_3$·C_5H_{12} (Figure 6). The torsion angles Pt−P−P−Pt and the Pt···Pt distances for the two conformers are different (Pt1−P1−P2−Pt2 = 36.05° and Pt1···Pt2 = 3.292 Å in the syn form; Pt3−P3−P4−Pt4 = −129.97° and Pt3···Pt4 = 5.60 Å in the anti form). The shorter Pt···Pt distances in the syn form have been similarly encountered in structures of the related cyclometalated Pt(II) complexes [(C^N^N)$_2$Pt$_2$(*μ*-dppm)](ClO$_4$)$_2$ (3.270 Å),[16g] [(C^N^N)$_2$Pt$_2$(*μ*-dppm)](ClO$_4$)$_2$·5H_2O (3.245 Å),[16h] and [(C^N^N)$_3$Pt$_3$(*μ*-dpmp)](ClO$_4$)$_3$·H_2O (3.190−3.400 Å; dpmp = bis(diphenylphosphinomethyl)phenylphosphine).[27b] In the crystal structure of **4a**·6$CHCl_3$·C_5H_{12}, there are extensive intra- and intermolecular C−H···π interactions between the molecules ($d_{C-H\cdots C}$ = 2.336−2.886 Å), C−H(solvent)···π interactions ($d_{C-H\cdots C}$ = 2.340−2.706 Å), and C−H···X contacts ($d_{C-H\cdots X}$ = 2.952−3.084 Å), as well as $\pi\cdots\pi$ stacking contacts ($d_{C\cdots C}$ = 3.255−3.329 Å). Interestingly, viewed along the *c*-axis,

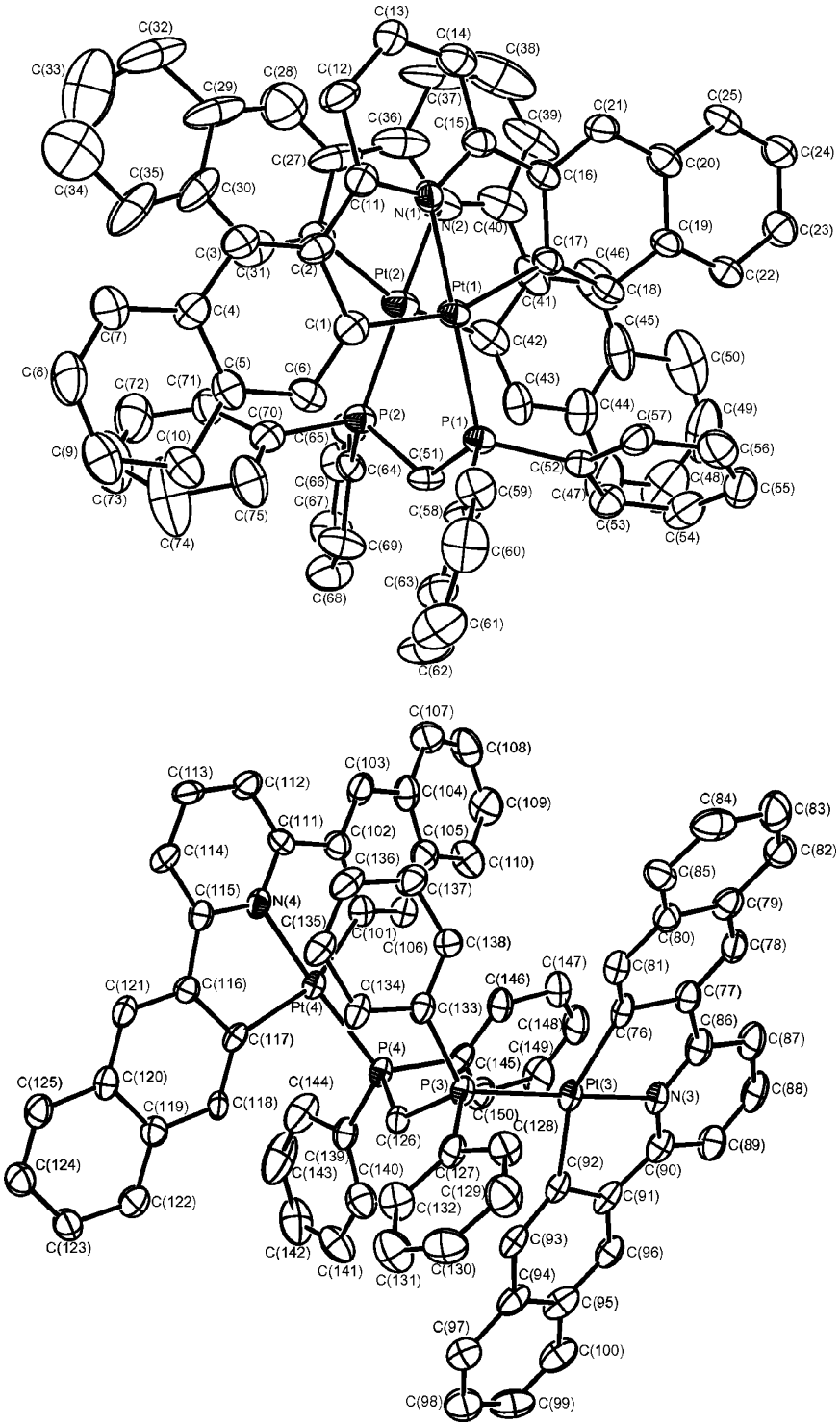

Figure 6. Perspective view of *syn*- (top) and *anti*-**4a** (bottom) (hydrogen atoms are omitted for clarity).

continuous solvent channels with aperture size of ca. 6.5 Å × 4.3 Å (estimated from the diagonal atom pairs C83···C108 and C137(x,y,z)···C137($-x,-y,-z$)) are found (Figure 7). A similar structural arrangement was also obtained when crystals of **4a** were prepared from a THF/*n*-C_5H_{12} solution (in this case, the solvent channels are occupied by THF molecules). Apart from the C−H···π interactions ($d_{C-H\cdots C}$ = 2.746−2.898 Å), some C−H···O weak hydrogen bonds ($d_{C-H\cdots O}$ = 2.658−2.681 Å) are observed between the O atom of THF molecules and the H atoms of **4a**. The structure and crystal packing diagram for **4a**·6.5THF are depicted in Figure S6 in the Supporting Information.

Unlike **4a**, the crystal structures of **4b**·2$CHCl_3$, **4c**·3CH_2Cl_2, and **4d**·2$CHCl_3$ have smaller percent void volumes (32.2% in **4a**, 16.7% in **4b**, 19.6% in **4c**, and 24.6% in **4d**, as calculated by the PLATON program[38]), with the voids having different aperture sizes (3.0 Å × 6.3 Å in **4b**, 2.8 Å × 7.4 Å in **4c**, and 2.0 Å × 4.6 Å in **4d**). These voids may be regarded as solvent cavities or clefts embedded inside the crystal structures; however, their sizes are much smaller than those found in the

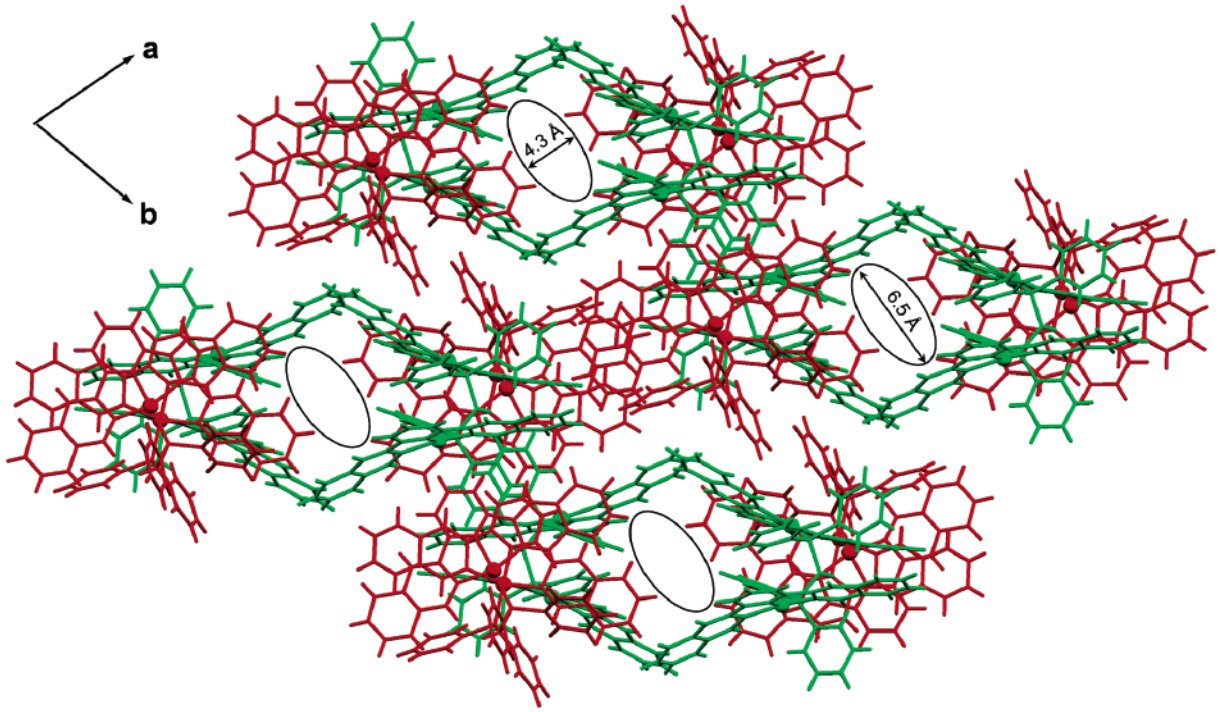

Figure 7. Porous molecular framework of **4a**·6$CHCl_3$·C_5H_{12} viewed along the *c*-axis. (The syn and anti conformers are colored as red and green, respectively, and solvent molecules are omitted for clarity.)

4a·6$CHCl_3$·C_5H_{12} crystals. The solvent channels in **4a** appear to be more accessible for solvent molecules to enter and exit, whereas the solvent molecules in the crystal structures of **4b**−**d** are "trapped".

Only one conformation—the syn form for **4b** and **4c** and the anti form for **4d**—was observed in the crystal structures of **4b**−**d**. Perspective views and crystal packing diagrams of **4c** and **4d** are depicted in Figures 8 and 9, respectively. Complex **4c**, which contains a 4-bromophenyl substituent on the cyclometalated ligand, has a staggered syn conformation with a small torsion angle α(Pt−P−P−Pt) of −0.71° (in contrast with −34.28° and −120.28° found for **4b** and **4d**, respectively). In this complex, the intramolecular Pt···Pt (d = 3.441 Å) and π···π (d = 3.337−3.397 Å) distances are longer than those in **4a**,**b**, and there is significant Br lone-pair repulsion, as manifested by the Br···Br separation (4.177 Å) being larger than the sum of the van der Waals radii (ca. 3.7 Å). In the crystal structure of **4d**·2$CHCl_3$, the anti form is presumably stabilized by weak intermolecular hydrogen bonds[37] [C−H···F] ($d_{C-H\cdots F}$ = 2.497−2.831 Å) involving the F atoms of the 3,5-difluorophenyl substituent.

Comparative PXRD of Solvated and Desolvated Complexes. The structures of desolvated solid forms of **4a**−**d** and the related [(C^N^C)$_2$Pt$_2$(μ-dppm)][27a] complexes were examined by PXRD. All the desolvated solids diffracted X-ray radiation moderately up to a maximum 2θ angle of ca. 36°. Indexing the experimental PXRD pattern for desolvated **4a** gave initial unit cell parameters that were subsequently refined, with the results listed in Table 4. The 2θ values of the diffraction peaks for the fundamental reflections [100], [010], and [001] are significantly deviated from those calculated using the crystal structure of **4a**·6$CHCl_3$·C_5H_{12}. For example, the 2θ values for the [100] reflection for the desolvated and solvated structures of **4a** are 5.877° and 5.297°, respectively, revealing a shortening of the crystallographic *a*-axis upon removal of occluded solvent molecules (Figure S8 in the Supporting Information). Whereas angular shifts for the [010] and [001] reflections were less apparent (2θ values for [010] and [001] for the solvated (desolvated) form are 4.619° (4.604°) and 4.417° (4.242°), respectively). Based on the unit cell parameters of the desolvated structure, there is a prominent contraction along the *a*-axis direction, with a reduction of the unit cell volume from 7374 to 6188 Å^3. The desolvated structure was solved and refined by the restrained Rietveld method, in which the molecular orientations of the syn and anti forms of **4a** were determined. The refined desolvated structure gave a calculated PXRD pattern that matched the experimental one (Figure S9 in the Supporting Information). On the other hand, the experimental PXRD pattern for desolvated solid [(C^N^C)$_2$Pt$_2$(μ-dppm)][27a] resembled the one calculated using the crystal data for [(C^N^C)$_2$Pt$_2$(μ-dppm)]·$CHCl_3$[27a] (Figure S10 in the Supporting Information). Indexing of the former gave the following unit cell parameters: a = 11.367 Å, b = 12.309 Å, c = 18.704 Å; α = 82.03°, β = 75.44°, γ = 70.53°; V = 2386 Å^3. These values are only slightly different from those reported for the $CHCl_3$ solvated structure (a = 11.605 Å, b = 12.509 Å, c = 18.795 Å; α = 82.35°, β = 75.11°, γ = 71.57°; V = 2497.7 Å^3).[27a] The change in the unit cell volume (ca. 6%) of the [(C^N^C)$_2$Pt$_2$(μ-dppm)]·$CHCl_3$[27a] crystal upon desolvation is relatively small. For the desolvated solids **4b**−**d**, there are less apparent peak position shifts (in 2θ) and variations of diffraction peak intensities between the experimental PXRD patterns for the desolvated solid and the ones calculated from the solvated single-crystal structures. For **4c**, a small background hump (ca. 5−12° (2θ)) in the experimental PXRD pattern was found, presumably due to an irreversible structural change of the molecular framework leading to a reduction of intensity and broadening of the diffraction peaks.

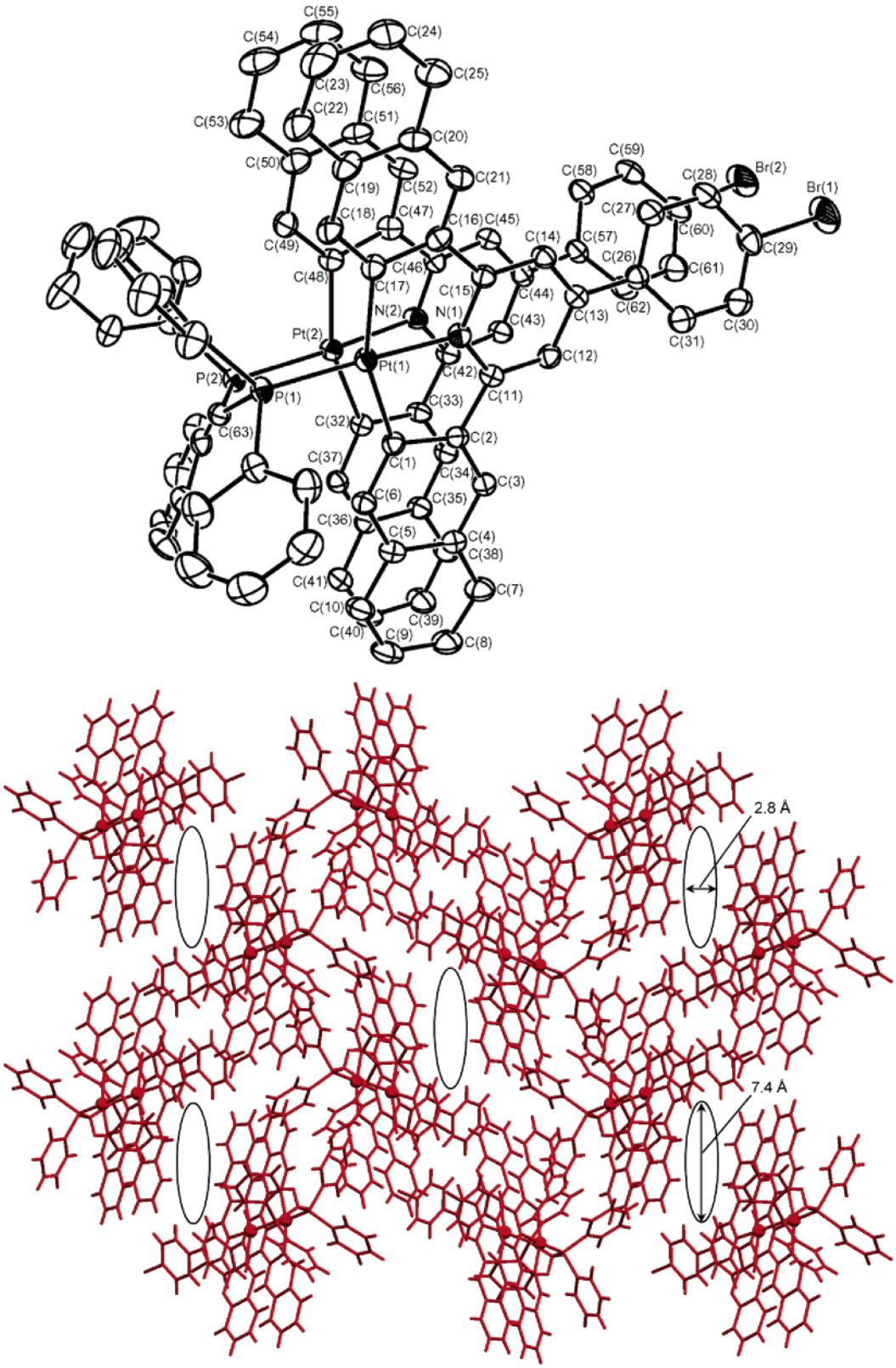

Figure 8. Perspective view of **4c**·3CH_2Cl_2, showing the staggered conformation (top) and solvent cavities in the packing diagram viewed from the *a*-axis (bottom) (solvent molecules are omitted for clarity).

General Remarks

The PXRD studies reveal that there are significant structural differences between the solvated and desolvated forms of **4a**. In the desolvated form, there is a more condensed packing of molecules, with alternating stacking of layers of syn- (red) and anti-form (green) **4a** molecules along the [100] direction (Figure 10). The solvent channels found in the solvated structure of **4a** are no longer present in the desolvated structure, and the solvent void spaces are occupied by the naphthyl groups of *anti*-[(R-C^N^C)$_2$Pt$_2$(μ-dppm)] molecules. Consistent with this observa-

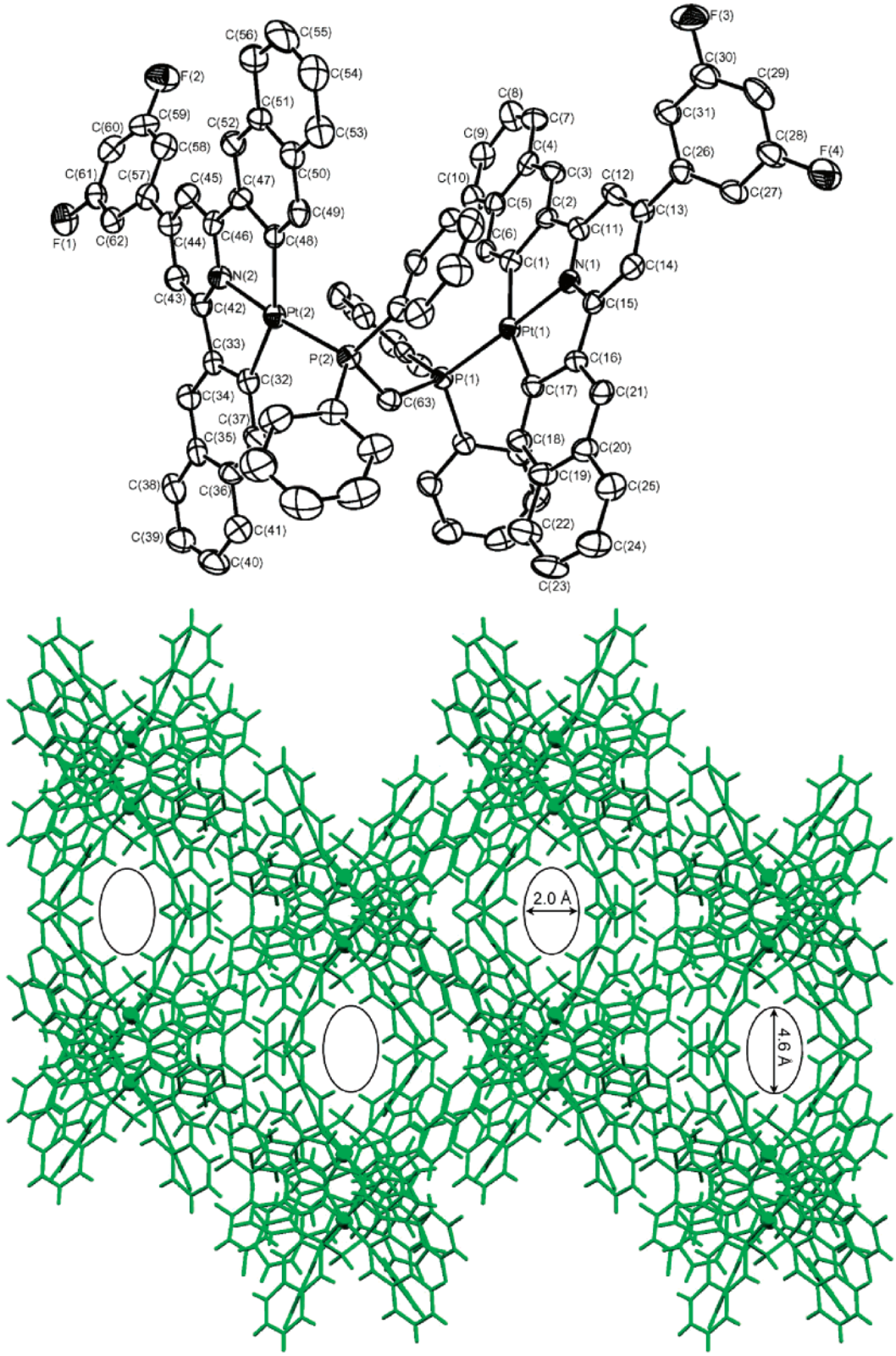

Figure 9. Perspective view of **4d**·2$CHCl_3$ (top) and the solvent cavities in the packing diagram viewed from the *c*-axis (bottom) (solvent molecules are omitted for clarity).

tion, a low surface area of 1.45 ± 0.1 m^2/g (measured by the Brunauer−Emmett−Teller method[40]) for the desolvated solid **4a** was found, indicating a non-porous nature. Going from the solvated to desolvated structures, there is increased molecular aggregation between the syn and anti forms of [(R-C^N^C)$_2$-Pt_2(μ-dppm)], with the approximate separation between the C49 and C126 atoms decreasing from 6.2(1) (solvated form) to 4.1(6) Å (desolvated form). Pt···Pt contact distances in the syn form

(40) Brunauer, S.; Emmett, P. H.; Teller, E. *J. Am. Chem. Soc.* **1938**, *60*, 309−319.

Table 4. Structural Refinement of Desolvated **4a** Using PXRD Data[a]

crystal system	triclinic
space group	$P\bar{1}$
a, Å	15.498(2)
b, Å	19.332(2)
c, Å	21.308(2)
α, deg	90.56(1)
β, deg	102.22(1)
γ, deg	96.99(1)
V, Å^3	6188.6(13)
Z	2
formula weight, g mol^{-1}	2866.76
$2\theta_{max}$, deg	3−50
no. data points collected, $y_{i,o}$	2350
no. refined variables, N_{var}	848
no. restraints used	1048
R_p	0.0797
R_{wp}	0.1123
R_{wp} (expected)	0.1042
goodness-of-fit, χ^2	2.13
max [shift/esd]^2 (mean)	0.55 (0.04)

[a] $R_p = \sum|y_{i,o} - y_{i,c}|/\sum|y_{i,o}|$; $R_{wp} = [\sum w_i(y_{i,o} - y_{i,c})^2/\sum w_i(y_{i,o})^2]^{1/2}$; expected $R_{wp} = R_{wp}/\chi^2$; $\chi^2 = \sum w_i(y_{i,o} - y_{i,c})^2/(N_{obs} - N_{var})$, where $y_{i,o}$ and $y_{i,c}$ are the observed and calculated intensities at point *i* of the profile respectively, N_{obs} is number of theoretical peaks in the considered range, and N_{var} is number of the refined parameters. Statistical weight w_i is normally taken as $1/y_{i,o}$.

increase slightly from 3.29(3) to 3.40(3) Å, while the Pt(3)···Pt(4) distance in the anti form decreases from 5.68(2) to 5.40(3) Å. The torsion angle α(Pt1−P1−P2−Pt2) increases from 36(1)° to 40(1)°, and α(Pt3−P3−P4−Pt4) decreases from −130(1)° to −120(1)°. Similar to the solvated structure, the syn and anti forms of **4a** in the desolvated structure are also held in place by extensive intermolecular C−H···π (d = 2.27−2.92(2) Å) and π···π (d = 3.20−3.47(2) Å) interactions (Table S2 in the Supporting Information).

On the basis of these findings, we propose that the closer aggregation of *syn*- and *anti*-[(R-C^N^C)$_2$Pt$_2$(μ-dppm)] molecules in the desolvated solid **4a** may be the reason for the quenching of the excimeric $^3\pi\pi^*$ emission (λ_{max} = 602 nm) from the cyclometalated R-C^N^C ligand. A possible mechanism for this quenching may involve intermolecular dipole−dipole interactions. As the VOC molecules enter the crystal structure of desolvated **4a**, the unit cell volume expands and the separation between the [(R-C^N^C)$_2$Pt$_2$(μ-dppm)] molecules increases, leading to a decrease in the quenching and a restoration of emission intensity to that found in the solvated solid **4a**. The constraints imposed by the size and hydrophobic nature of the solvent channels in the solvated **4a** structure may affect the vapoluminescent properties. The desolvated solid **4a** is sensitive to the VOC molecules $CHCl_3$, CH_2Cl_2, acetone, and THF, all of which may form C−H(solvent)···π and/or C−H···O(solvent) interactions with the [(R-C^N^C)Pt] moieties. The polar acetonitrile, methanol, and ethanol molecules are not hydrophobic enough, and the benzene, toluene, and *n*-hexane molecules may be too large to fit into the solvent channels in solvated **4a**, leading to insignificant changes in the emission intensity for these VOC molecules. It is important to note that the emission of desolvated **4a** shows little enhancement upon exposure to the small, non-hydrogenated solvents, CCl_4 ($I_{voc}/I_{desolvate} \approx 6$) and CS_2 ($I_{voc}/I_{desolvate} \approx 7$). Apart from the size and the hydrophobic nature of the solvent molecules, we conceive that the C−H(solvent)···π and/or C−H···O(solvent) interactions play key roles in the vapoluminescent behavior of **4a**.

In the literature, several mechanisms have been proposed for reversible vapoluminescence.[19−23] It has been suggested that the facile internal reorganization of molecules upon transition from the solvated to the desolvated structures may be thermodynami-

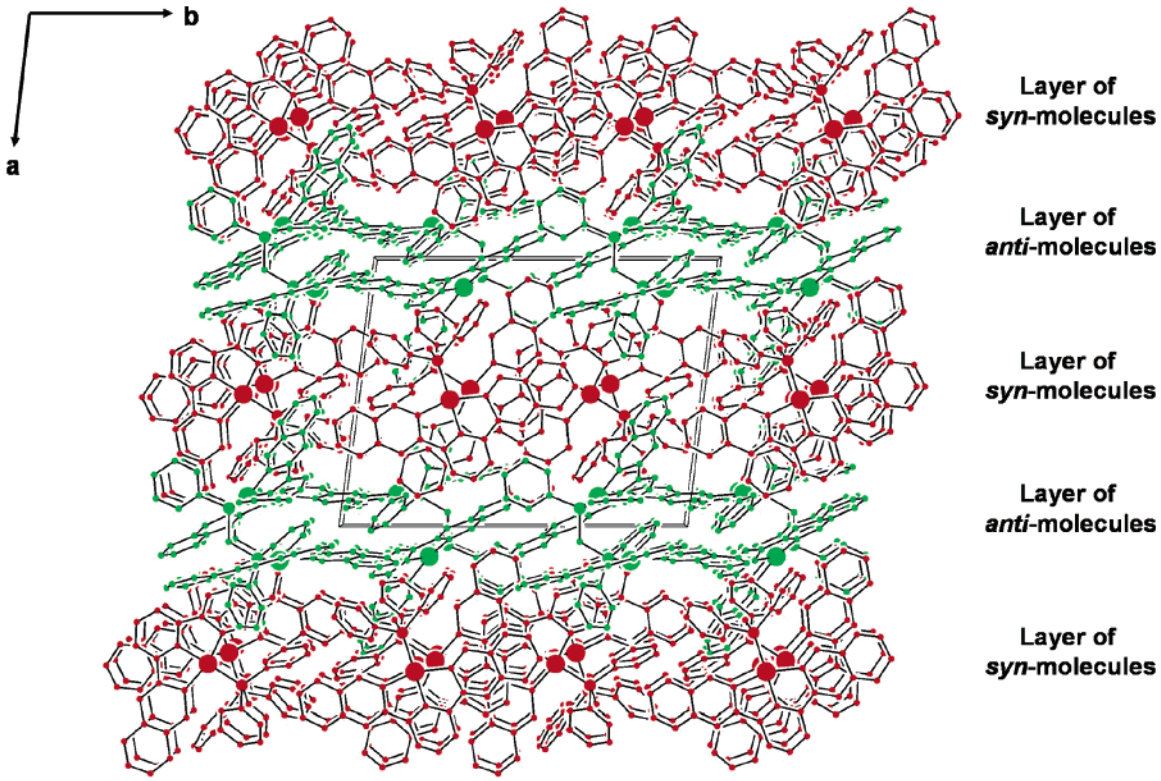

Figure 10. Molecular packing within desolvated **4a** viewed from the *c*-axis (hydrogen atoms are omitted for clarity).

cally driven by a minimal Gibbs free energy change. Therefore, the sum of the enthalpies due to the formation of a condensed desolvated structure, combined with the entropy gained from the desolvation of the solvated molecular framework, should match the stabilization enthalpies due to the complex−complex (C−H···π and π···π interactions), complex−solvent (such as C−H···X), and solvent−solvent (i.e., X···X) interactions. The presence of accessible solvent channels in the solvated structure, as well as cooperative weak interactions, particularly C−H···π interactions, would facilitate the structural changing process. Upon exposure to air, solvent molecules would escape through the solvent channels for complete desolvation.

Among the complexes **4a**−**d**, the unique vapoluminescent behavior of **4a** is attributed to its molecular structure and crystal packing. The equimolar amounts of the syn and anti forms of the complex serve as optimal structural building blocks for a porous molecular framework. The accessible solvent channels of optimal aperture size/shape are large enough to allow the passage of the VOC molecules. In addition, the larger void volume found in the solvated structure of **4a** is the reason behind the large structural changes that occur when the occluded solvent molecules are removed. The reported crystal structures of the vapoluminescent crystals $[(C\hat{}N\hat{}C)_2Pt_2(\mu\text{-dppm})]$[27a] and $[(^tBu_2bpy)Pt(C{\equiv}CR)_2]$ (R = *p*-pyridyl)[23c] have also been re-analyzed in this work: these two systems also contain accessible solvent channels with diameters >4 Å in one lattice direction.

Analysis of the solvated X-ray crystal structures of **4a**−**d** revealed extensive intra- and intermolecular interaction networks. Relatively strong C−H(solvent)···π interactions were observed in the crystal structures, underpinning the unique vapoluminescent properties of **4a**. Interestingly, non-covalent C−H···π and π···π stacking interactions were also found in the desolvated structure of **4a**. These interactions may stabilize the lattice structure, preserving the crystallinity of the desolvated structure of **4a**.

Upon exposure to VOCs, intermolecular attractions between the Pt complexes and solvent molecules through C−H···X and X···X interactions may be responsible for restoring the solvated structure. Especially for halogenated VOCs, these interactions could become strong enough to direct the restoration of the molecular framework to the solvated structure. However, it is likely that the re-solvation of the desolvated **4a**−**d** and $[(C\hat{}N\hat{}C)_2Pt_2(\mu\text{-dppm})]$[27a] solids proceeds at the solid/gas interfacial boundaries of the solid samples.

The molecular conformations (either syn or anti form) of the dinuclear complexes **4a**−**d** do not appear to be essential criteria for the vapoluminescent behavior. The solvated structure of **4a**·$6CHCl_3{\cdot}C_5H_{12}$ contains an equimolar mixture of the syn and anti forms of $[(R\text{-}C\hat{}N\hat{}C)_2Pt_2(\mu\text{-dppm})]$. On the other hand, the syn forms of **4b**,**c** and the anti form of **4d** are not vapoluminescent toward VOCs. Formation of a porous molecular framework in the crystal structures with accessible solvent channels of suitable size and shape is affected by the aryl substituents on the R-C^N^C ligands. The crystal packing of solvated **4a**·$6CHCl_3{\cdot}C_5H_{12}$ and **4a**·6.5THF is coincidentally optimized at both the molecular and supramolecular levels for vapoluminescence behavior.

Conclusions

Mononuclear and dinuclear cyclometalated [(R-C^N^C)Pt] complexes were prepared and structurally characterized. The extended π-conjugated naphthyl-substituted cyclometalated ligands of these dinuclear Pt(II) complexes are central to their photophysical properties. Accessible solvent channels and the presence of weak and reversible non-covalent C−H···π, π···π, C−H···X, and X···X interactions account for the vapoluminescent behavior of **4a**. These extensive weak and reversible interactions tailor the supramolecular assembly of molecular frameworks and fundamentally affect the emission properties of Pt(II) complexes in the solid state. The sensitivity of the emission properties of square planar Pt(II) complexes is the basic operating principle behind their application as molecular VOC sensory materials. PXRD is a powerful technique, providing invaluable insight into the structural differences between the solvated and desolvated forms of this class of vapoluminescent solids.

Acknowledgment. We are grateful for financial support from The University of Hong Kong (large-item equipment funding) and the University Development Fund, the Research Grants Council of the HKSAR, China [HKU 7039/03P]. S.C.F.K. acknowledges the receipt of a postgraduate studentship administered by the University of Hong Kong. S.S.-Y.C. acknowledges financial support from the award of a Postdoctoral Fellowship from the AoE Scheme [AoE/P-10/01]. We also thank Dr. M. C. W. Chan, Dr. R. M. Watt, and Dr. W. Y. Yu for helpful discussions, and Mrs. B. F. Y. Yan and Mrs. C. S. F. Cheung for experimental assistance.

Supporting Information Available: Experimental procedures and characterization of **1a**−**d**, **2a**−**d**, **3**, and **4a**−**d**; crystallographic data for **2a**−**c**; summary of intra- and intermolecular non-covalent contact distances of **2a**−**c**, **4a**−**d**, and desolvated **4a** (Table S2); simulated and experimental $^{31}P\{^1H\}$ NMR spectra of **4b** (Figure S1); plot of emission intensity versus temperature (103−163 K) of **4b** in 2-MeTHF (Figure S2); correlation plot between quantum yield Φ_{ss} and relative intensity ($I_{voc}/I_{desolvate}$) of the desolvated solid **4a** upon exposure to various VOCs (Figure S3); perspective views and molecular packing diagrams of **2b**·$CHCl_3$, **2c**·$2CH_2Cl_2$, **4a**·6.5THF, and **4b**·$2CHCl_3$ (Figures S4−S7); experimental PXRD pattern of the desolvated form and calculated PXRD of the solvated form of **4a** and $[(C\hat{}N\hat{}C)_2Pt_2(\mu\text{-dppm})]$ based on their single-crystal data (Figures S8−S10); UV−vis absorption spectra of **2a**−**d** in CH_2Cl_2 solutions (Figure S11); solid-state emission spectra of **2a**−**d** at 298 K (λ_{ex} = 350 nm) (Figure S12); emission spectra in the solid state at 77 K and in 2-MeTHF glassy solutions of **2a** (Figure S13), **2b** (Figure S14), **2c** (Figure S15), and **2d** (Figure S16); UV−vis absorption spectra of **3** (Figure S17) and **4a**−**d** (Figure S19) in CH_2Cl_2 solutions; solid-state emission spectra of **4a**−**d** at 298 K (λ_{ex} = 350 nm) (Figure S20); emission spectra in the solid state at room temperature and 77 K and in 2-MeTHF glassy solution at 77 K for **3** (Figure S18), **4a** (Figure S21), **4b** (Figure S22), **4c** (Figure S23), and **4d** (Figure S24); and crystallographic information files (CIF) of **2a**, **2b**·$CHCl_3$, **2c**·$2CH_2Cl_2$, **4a**·$6CHCl_3{\cdot}C_5H_{12}$, **4a**·6.5THF, **4b**·$2CHCl_3$, **4c**·$3CH_2Cl_2$, **4d**·$2CHCl_3$, and desolvated **4a**. This material is available free of charge via the Internet at http://pubs.acs.org.

JA061422X